AIMS Materials Science, 13(5): 913–938.
DOI: 10.3934/matersci.2026043
Received: 18 August 2026
Revised: 07 September 2026
Accepted: 22 September 2026
Published: 15 October 2026

https://www.aimspress.com/journal/Materials

Research article

Glass-phase microstructure and He/Ne separation performance of cenosphere-based microspherical membranes

Elena V. Fomenko[1,*], Timur Yu. Ivanenko[1], Sergey V. Kukhtetskiy[1], Nikolay P. Shestakov[2], Alexander S. Krylov[2], Leonid A. Solovyov[1] and Tatiana A. Vereshchagina[1]

[1] Institute of Chemistry and Chemical Technology, Federal Research Center, Krasnoyarsk Science Center of the Siberian Branch of the Russian Academy of Sciences, Akademgorodok 50/24, 660036 Krasnoyarsk, Russia

[2] L.V. Kirensky Institute of Physics, Federal Research Center, Krasnoyarsk Science Center of the Siberian Branch of the Russian Academy of Sciences, Akademgorodok 50/38, 660036 Krasnoyarsk, Russia

* **Correspondence**: Email: fom@icct.ru.

Supplementary

The spin-state splitting is reported both as the difference of electronic energies and with the zero-point correction included Eqs S1 and S2:

$$\Delta E = E_{el}\left(S = {}^{1}/_{2}\right) - E_{el}\left(S = {}^{5}/_{2}\right) \tag{S1}$$

$$\Delta E_0 = \Delta E + \left[ZPE\left(S = {}^{1}/_{2}\right) - ZPE\left(S = {}^{5}/_{2}\right)\right] \tag{S2}$$

A positive value indicates that the high-spin state is the ground state. The corresponding thermal population ratio follows from the Boltzmann distribution, the degeneracy factors being $g = 2S + 1$, Eq S3:

$$\frac{n_{LS}}{n_{HS}} = \left(\frac{g_{LS}}{g_{HS}}\right) e^{-\Delta E_0/RT} \tag{S3}$$

With $\frac{g_{LS}}{g_{HS}}$ = 2/6 and ΔE_0 = 21.7–27.1 kcal/mol the low-spin population ratio is order of 10^{-20} at 298 K and 10^{-5} at 1300 K. The low-spin state is therefore thermally inaccessible under any conditions relevant to the annealing treatment.

For an exact spin eigenfunction the $\langle S^2 \rangle$ reduces to the ideal value S(S+1). The extent of contamination is quantified by the absolute and relative deviations Eq S4:

$$\Delta\langle S^2\rangle = \langle S^2\rangle_{calc} - S(S+1), \delta = \frac{\Delta\langle S^2\rangle}{S(S+1)} \times 100\% \tag{S4}$$

A deviation below roughly 10% of the ideal value is usually regarded as acceptable. As shown in Table S1, the high-spin solutions satisfy this criterion (δ = 0.1–3.8%), whereas the low-spin solutions are contaminated by 150–265%—their $\langle S^2 \rangle$ values lie closer to the quartet ideal of 3.75 than to the doublet ideal of 0.75. the low-spin results are consequently reported for completeness only and are excluded from the interpretation.

Non-planarity is reported as the root-mean-square deviation of the atoms from the least-squares plane of the fragment. The plane is obtained by singular value decomposition of the centred coordination matrix; it's normal n is the right singular vector associated with the smallest singular value, and Eq S5:

$$RMS_{out-of-plane} = \sqrt{[(1/N)\sum_i (r_i n)^2]} \tag{S5}$$

A value close to zero denotes a strictly planar fragment; values of the order of 1 Å denote a strongly puckered ring.

Within the double-harmonic approximation the intensity of mode k is governed by the square of the dipole-moment derivative taken along the mass-weighted normal coordinate Q_k (Eq S6):

$$A_k = \left({}^{N_A\pi}/_{3c^2}\right)\left|{}^{\partial\mu}/_{\partial Q_k}\right|^2 \tag{S6}$$

with N_A the Avogadro constant. Physically, A_k is the integrated molar absorption coefficient, that is, the absorption of the band integrated across the wavenumber axis (Eq S7):

$$A_k = \left(1/n\iota\right) \int ln\left(\frac{I_0}{I}\right) d\nu \quad \text{(S7)}$$

where n is the amount-of-substance concentration, ι the optical path length and ν the wavenumber.

Dimensional analysis gives cm/mol, that is, length per amount of substance. It should be emphasised that km/mol is a unit of length per mole and not of energy. Because A_k is proportional to $(\partial\mu/\partial Q_k)^2$, a normal mode that does not modulate the dipole moment carries zero intensity irrespective of its frequency or of the energy stored in it. Several ring-breathing modes of the pristine $(SiO)_n$ clusters are IR-silent for precisely this reason.

The intensity summed over a spectral window is obtained by adding the intensities of all IR-active modes falling within it (Eq S8):

$$I(\nu_1, \nu_2) = \sum_k A_k \text{ for } \nu_1 \leq \nu_k < \nu_2 \quad \text{(S8)}$$

The empirical scaling factor relating a calculated band to its experimental counterpart is defined as $S = {\nu_{exp}}/{\nu_{calc}}$. A physically sound cluster model yields a single value of s, typically between 0.95 and 1.00, for all bands. The spread obtained here (1.20, 0.88, 1.06 for TO_1, TO_2 and TO_3 respectively) indicates a structural rather than an anharmonic origin of the deviation. Absolute frequencies obtained from these models are not directly comparable with experiment: the scaling factors ${\nu_{exp}}/{\nu_{calc}}$ amount to 1.20 in the TO_1 region, 0.88 for TO_2 and 1.06 for TO_3, so that no single scaling factor exists. Comparison with experiment is therefore made differentially—through the shifts Δν and the intensity changes between a pristine ring and a ring of the same size containing a cation, and through the localisation of normal modes on specific structural fragments.

To determine which astructural unit is responsible for a given band, the fraction of the vibrational kinetic energy of mode k residing on a fragment F was computed from the mass-weighted Cartesian displacement $\nu_{k,a}$ (Eq S9):

$$L_k(F) = \sum_{a \in F} m_a \left|\nu_{k,a}\right|^2 / \sum_a m_a \left|\nu_{k,a}\right|^2 \quad \text{(S9)}$$

The sum in the numerator runs over the atoms of the fragment (both tetrahedral centres and the bridging oxygen atoms shared between them), the sum in the denominator over all atoms of the cluster. Values of L_k above about 0.8 indicate that the mode is essentially a localised vibration of that unit rather than a delocalised framework mode.

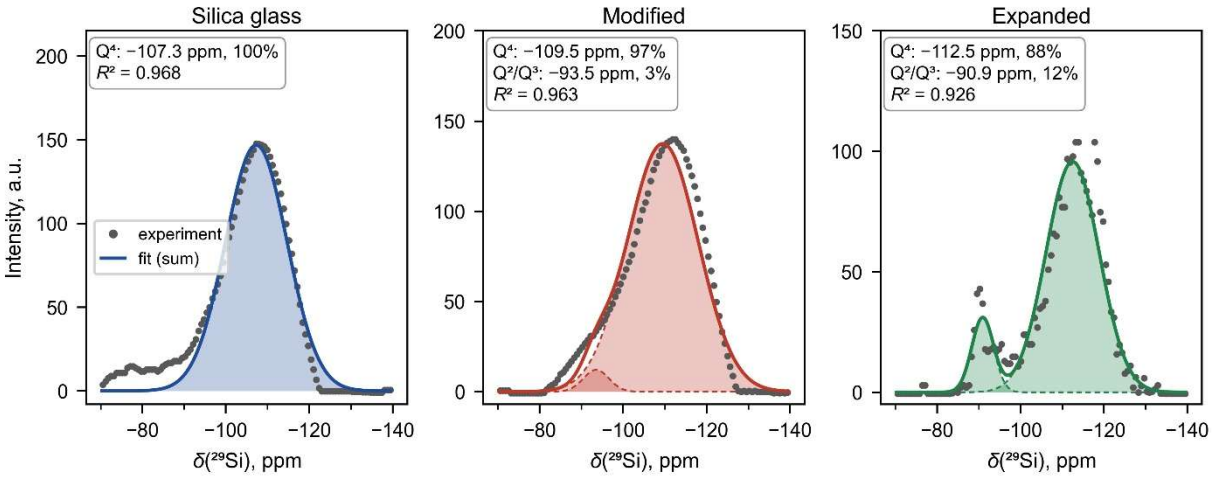


Figure S1. Deconvolution of ^{29}Si MAS NMR spectra into Q^n structural-unit contributions.

Table S1. Fe(III) spin-state energy disparities and concomitant spin contamination.

$(SiO)_n$ ring	ΔE, kcal/mol	ΔE_0 (ZPE corrected), kcal/mol	$<S^2>$ at S = 5/2	Ideal 8.750	δ, %	$<S^2>$ at S = 1/2	Ideal 0.75	δ, %
n = 6	22.72	23.42	8.762	8.750	0.1	1.877	0.750	150
n = 7	21.53	21.73	8.807	8.750	0.6	2.564	0.750	242
n = 8	26.99	27.10	9.080	8.750	3.8	2.741	0.750	265
n = 9	24.12	25.07	9.069	8.750	3.6	2.482	0.750	231

The high-spin state S = 5/2 is the ground state for every ring size, as expected for a d^5 Fe(III) centre in the weak ligand field of an oxygen environment. The low-spin solutions are heavily spin-contaminated.

Table S2. Bond length, angle and planarity.

System	d(Si–O), Å	Bridging-angle range, deg.	Cation coordination number	d(M–O), Å	$RMS_{out\text{-}of\text{-}plane}$ deviation, Å
$(SiO)_6$	1.647 ± 0.000	176–179	—	—	0.545
$(SiO)_7$	1.649 ± 0.004	148–173	—	—	0.648
$(SiO)_8$	1.652 ± 0.005	151–167	—	—	0.974
$(SiO)_9$	1.651 ± 0.006	152–175	—	—	1.053
$(SiO)_6$ + Al	1.617 ± 0.085	149–174	4	1.771	1.223
$(SiO)_7$ + Al	1.685 ± 0.125	86–166	3	1.772	1.181
$(SiO)_8$ + Al	1.732 ± 0.116	77–164	3	1.825	0.860
$(SiO)_9$ + Al	1.686 ± 0.094	88–174	2	1.694	0.910
$(SiO)_6$ + Fe (S = 5/2)	1.724 ± 0.076	99–176	4	2.069	0.002
$(SiO)_7$ + Fe (S = 5/2)	1.679 ± 0.088	95–179	2	2.267	0.205
$(SiO)_8$ + Fe (S = 5/2)	1.689 ± 0.075	83–177	3	2.095	0.605
$(SiO)_9$ + Fe (S = 5/2)	1.684 ± 0.072	94–174	3	2.110	0.873
$(SiO)_6$ + Fe (S = 1/2)	1.742 ± 0.126	94–171	4	1.980	0.001
$(SiO)_7$ + Fe (S = 1/2)	1.683 ± 0.092	95–176	3	2.280	0.013
$(SiO)_8$ + Fe (S = 1/2)	1.686 ± 0.070	82–177	3	2.076	0.661
$(SiO)_9$ + Fe (S = 1/2)	1.678 ± 0.079	84–170	3	2.085	0.966

The pristine rings form a monotonic series. In $(SiO)_6$ the Si–O–Si bridging angle are almost linear (mean 177.8°) and the ring is essentially planar; as n increases the angle relaxes toward 158–160°, a value typical of vitreous silica, and ring becomes progressively puckered. Incorporation of a cation broadens range dramatically, the lower limit falling to 77–88°, which reflects the formation of strained fragments. In the small rings Fe(III) acts as a template: the out-of-plane deviation of $(SiO)_6$ collapses from 0.545 to 0.002 Å, so that the ring becomes strictly planar with four-coordinated iron at its centre. The effect disappears in the larger rings, which are too wide to wrap around the cation.

Table S3. Integrated IR absorption intensity over the 100–400 cm^{-1} range, km/mol.

$(SiO)_n$	Initial	$+Al^{3+}$	$+Fe^{3+}$ (S = 5/2)	$+Fe^{3+}$ (S = 1/2)
n = 6	205	218	163	386
n = 7	148	442	203	167
n = 8	96	450	284	288
n = 9	141	335	182	262
Mean	147	361	208	276
Enhancement factor	1.00	2.45	1.41	1.87

Decomposition of the intensity over atoms shows that modes in which the cation participates by more than 15% account for only 0–84 km/mol of the total increase. The enhancement of far-infrared absorption is therefore caused by the activation of framework modes through symmetry breaking and

the formation of strained fragments, and not by metal–oxygen vibrations. This is why the excess absorption observed experimentally persists after the cations have been removed.

Table S4. Dominating Si–O stretching vibration in the pristine $(SiO)_n$ rings.

System	ν, cm^{-1}	I, km/mol	⟨Si–O–Si⟩, deg.
$(SiO)_6$	1031.7	2226	177.8
$(SiO)_7$	1000.8	2669	164.2
$(SiO)_8$	958.4	1993	158.3
$(SiO)_9$	956.1	2382	159.7

The monotonic red shift of the dominant stretching vibration with increasing ring size (1032 → 1001 → 958 → 956 cm^{-1}) is accompanied by relaxation of the mean bridging angle (177.8 → 164.2 → 158.3 → 159.7°). The shift therefore reflects the release of angular strain rather than the ring size as such.

Table S5. Dominating calculated mode in each spectral window.

System	100–300 cm^{-1} (I, km/mol)	300–500 cm^{-1} (I, km/mol) (TO_1)	500–650 cm^{-1} (I, km/mol) (cyclic, D_2 mode)	650–750 cm^{-1} (I, km/mol)	750–950 cm^{-1} (I, km/mol) (TO_2, 2-members)	950–1150 cm^{-1} (I, km/mol) (TO_3)	1150–1300 cm^{-1} (I, km/mol) (LO)
$(SiO)_6$	102 (0)	370 (91)	570 (38)	—	864 (0)	1032 (2226)	—
$(SiO)_7$	242 (14)	413 (77)	602 (27)	—	852 (5)	1001 (2669)	—
$(SiO)_8$	240 (22)	401 (85)	591 (35)	—	917 (458)	958 (1993)	—
$(SiO)_9$	241 (21)	403 (90)	625 (59)	—	909 (442)	956 (2382)	—
$(SiO)_6$ + Al	269 (66)	468 (199)	538 (122)	668 (59)	—	986 (2245)	1182 (712)
$(SiO)_7$ + Al	294 (49)	374 (144)	556 (253)	746 (451)	805 (137)	1045 (1430)	1170 (510)
$(SiO)_8$ + Al	154 (63)	434 (170)	510 (212)	692 (1148)	784 (672)	1013 (1303)	—
$(SiO)_9$ + Al	218 (53)	498 (186)	611 (144)	698 (276)	892 (336)	1021 (1851)	1152 (361)
$(SiO)_6$ + Fe (S = 5/2)	294 (23)	327 (76)	606 (944)	661 (651)	805 (702)	1103 (918)	—
$(SiO)_7$ + Fe (S = 5/2)	259 (58)	414 (285)	617 (420)	660 (59)	763 (800)	1003 (1204)	—
$(SiO)_8$ + Fe (S = 5/2)	299 (39)	336 (95)	618 (372)	738 (739)	825 (444)	1113 (914)	—
$(SiO)_9$ + Fe (S = 5/2)	242 (26)	445 (203)	616 (429)	699 (37)	809 (1095)	1101 (1035)	—
$(SiO)_6$ + Fe (S = 1/2)	265 (54)	474 (130)	624 (602)	689 (246)	833 (555)	1079 (949)	—
$(SiO)_7$ + Fe (S = 1/2)	252 (48)	402 (345)	606 (426)	657 (64)	790 (927)	1003 (1479)	—
$(SiO)_8$ + Fe (S = 1/2)	254 (11)	361 (62)	624 (278)	746 (911)	945 (398)	1109 (777)	—
$(SiO)_9$ + Fe (S = 1/2)	244 (70)	440 (143)	605 (384)	—	863 (562)	1100 (1052)	—

In the pristine $(SiO)_6$ and $(SiO)_7$ rings the 750–950 cm^{-1} region carries virtually no intensity (0 and 5 km/mol), whereas in every cation-containing system this region is strong (137–1095 km/mol). It is precisely this region that corresponds to the 700–950 cm^{-1} band discussed in the main text, which persists in the extended sample after the modifiers have been removed.

Table S6. IR modes of two-membered siloxane fragments.

Sample	Experimantal	Calculated	Difference
Modified (Al^{3+} in structure)	843 cm^{-1}	827.2 cm^{-1}—fragment Si–Al with common edge, localization 71%	+16 cm^{-1}
Expanded (Al^{3+} removed)	901 cm^{-1}	892.5 cm^{-1}—pure Si–Si fragment, localization 90%	+9 cm^{-1}
Band shift after Al^{3+} removed	+58 cm^{-1}	+65 cm^{-1}	–7 cm^{-1}



AIMS Press

© 2026 the Author(s), licensee AIMS Press. This is an open access article distributed under the terms of the Creative Commons Attribution License (https://creativecommons.org/licenses/by/4.0)